

Characterization of the Microstructure of A Breakout Steel Sample

Ignatius C. Okafor¹, Ben Lovell² and Douglas Ambrosio³

¹Product Metallurgist, Gerdau Long Steel North America, Jackson Mill, TN 38305

²Quality Manager, Gerdau Long Steel North America, Jackson Mill, TN 38305

³Improvement Facilitator, Gerdau Long Steel North America, Jackson Mill, TN 38305

*Corresponding Author

Ignatius C. Okafor, Product Metallurgist, Gerdau Long Steel North America, Jackson Mill, TN 38305

Submitted: 2023, Sep 30; Accepted: 2023, Oct 17; Published: 2023, Nov 13

Citation: Okafor, I. C., Lovell, B., Ambrosio, D. (2023). Characterization of the Microstructure of a Breakout Steel Sample. *J App Mat Sci & Engg Res*, 7(2), 150-165.

Abstract

The microstructure of a continuously cast breakout of low carbon steel has been studied using optical microscopy; SEM/EDS and EBSD analysis techniques. SEM and EBSD studies were carried out on two different locations on one sample piece and the resulting room temperature grains were found to be mostly BCC α -ferrite phase. Their orientations (using Euler angles) were determined. No meaningful amount of FCC phase was indexed after two patterns indexed on the two locations of the sample piece. The FCC comprised only 0.02% to 0.08% of the total patterns indexed. EBSD maps for the two locations, along with pole figures and grain size charts were deduced for the BCC phase. Volume fraction of the phase was estimated. Reconstruction of the Prior Austenite Grain Boundary was made from the alpha grains data using AztecWave software (AZtecCrystal). Only a small amount of the prior austenite grain boundaries was determined suggesting that the size of the parent grains were significantly larger than the map area in each case.

1. Introduction

Steel strand rupturing is a common issue in continuous casting of both billets and slabs. Unlike in the slab casting industry where various technologies have been developed to predict possible breakouts, the billet industry counterpart is handicapped by the mold geometry that is the size and number of molds needed in each caster (4 to 8 and counting). The technology therein is not as robust most likely due to cost.

When this breakout occurred therefore, we thought we could learn a few things from both the cause of the event and the metallurgy associated with the said steel chemistry. The theory and processes associated with steel breakouts have been well documented in literature. Savage and Pritchard postulated that the steel strand shell tears near the meniscus when the upper part of the shell adheres to the mold [1]. Another author suggested that when mold powder is used as a lubricant, it forms a high carbon area in the solidifying shell which is weak and inhibits proper flux flow and that initiates a tear in the shell [2]. The use of oil lubrication offers a different challenge mostly coming from inadequate oil flow. The lack of enough oil distribution and uneven lubrication of the solidifying steel shell causes sticking to the mold. In general, it is known that the following parameters do influence breakouts in billet steel manufacturing.

a) Lubrication Oil Flow rate

- b) Relative humidity and Hydrogen presence in the atmosphere
- c) Liquid steel temperature
- d) Mold level fluctuation
- e) Mold oscillation
- f) Steel composition- peritectic or otherwise
- g) Casting speed and so steel residence time in the mold
- h) Uneven strand cooling.

This work took a quick look at what may have caused the breakout and proposed preventive actions going forward. This is in an internal report.

The work also aims to characterize the room temperature grain structure from the solidified shell and also attempted a reconstruction of the prior austenite grain size.

Phase transformation from the austenite phase (γ) to ferrite phase (α) is responsible for control of microstructures of steel products and the mechanical properties. Prior austenite microstructure (before transformation) influences the said mechanical properties. Therefore, information about the prior austenite microstructure has become of much interest.

Consequently, methods to acquire information about prior austenite microstructures have been assiduously researched and developed [3-7]. Many commercially available computer programs (including MTEX8 and Aztec9 Wave; Aztec Crystal) now exist that enable reconstruction of prior austenite

microstructure using data of crystal orientations. The principle is based on Euler angles' crystal orientation relationships. Information exists in the literature for the use of these methods on martensite and bainitic starting microstructures, but not much on low carbon low alloy steels. The paucity of information in the literature for this class of steel served as a major motivation for this aspect of the work. Maps derived from EBSD techniques offer the possibility of directly inferring the parent (Y) microstructure from the inherited one [10-12]. In this work we have used EBSD data to reconstruct the prior austenite grain size using the AztecWave Software in low carbon low alloy steel.

2. Metallography

2.1 Material

Samples from low carbon low alloy steel used in this study were obtained from a functioning steel mill. The said steel is from a breakout heat. The breakout was reported to be because of shell sticking to the mold during continuous casting. The samples were therefore completely air cooled in uncontrolled ambient atmosphere.

2.2 Microstructure

Microstructural studies were carried out in longitudinal and transverse directions. Samples were cut using the Buehler abrasive cut off machine. They were then mounted in Bakelite using the water- cooled LECO MX 500.

Mounted samples were polished using the STRUERS Tegramin 25 polisher. They were ground through Piano's 200, and 1200 metallic grits and polished thereafter through various steps to

the following micron sizes: 9 μm ; 3 μm ; 1 μm and $\frac{1}{4}$ μm using Diamond Suspension in that order. Samples were washed out with water and etched in 2% - 3% Nital. Etched samples were studied under a Zeiss Microscope at magnification 200x.

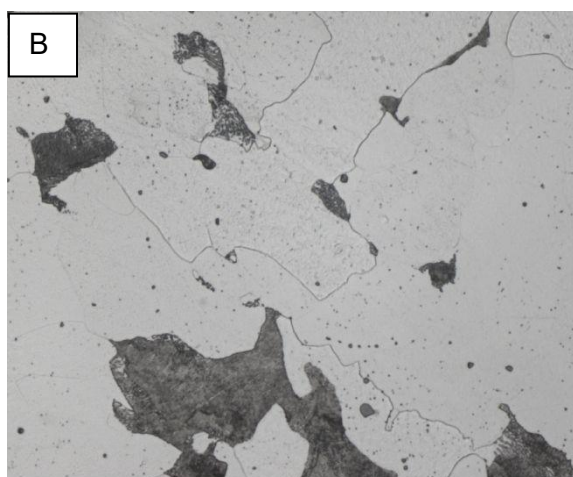
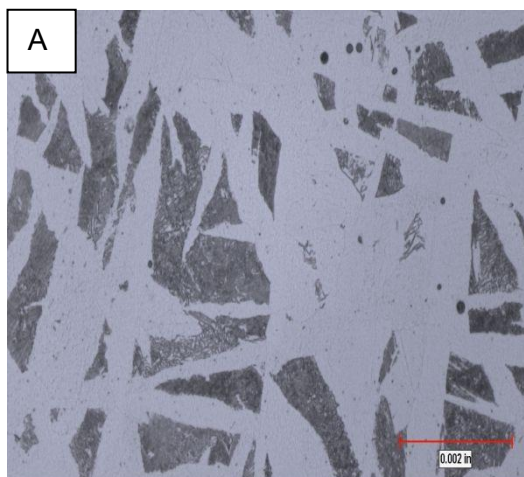
2.3 SEM – EBSD STUDY

SEM and EBSD data were obtained at the The McCrone Group laboratory. For the scanning electron microscopy (SEM) imaging, EBSD and X-ray spectroscopy (EDS) analyses, samples were prepared using standard grinding and polishing procedures. The mechanically polished surface was etched in Nital-2% concentrated HNO_3 in ethanol for a few seconds for SEM. Each sample was further polished using the Leica TIC3X triple ion beam polisher. Even though the polish was considered good it still had about 15% zero solutions. That is areas producing no patterns or unindexable patterns, which were likely due to variations in the surface finish. The SEM equipment was set at Accelerating Voltage of 20.22Kv; Specimen Tilt (degree) of 70.00; Hit Rate of 78.88% and Speed of Acquisition set at 40.32Hz.

3 Results

3.1 Optical Microscopy

The microstructure of the sample showed various patterns that ranged from typical dendritic morphology (see Fig. 1 A, F and G) through as-cast solidified ferrite structure. However, the primary microstructure is acicular ferrite (Fig. C, D, and E) and granular bainite with some allotriomorphic ferrite (Fig. 1 C, D, and E). Some of microstructures are shown below.



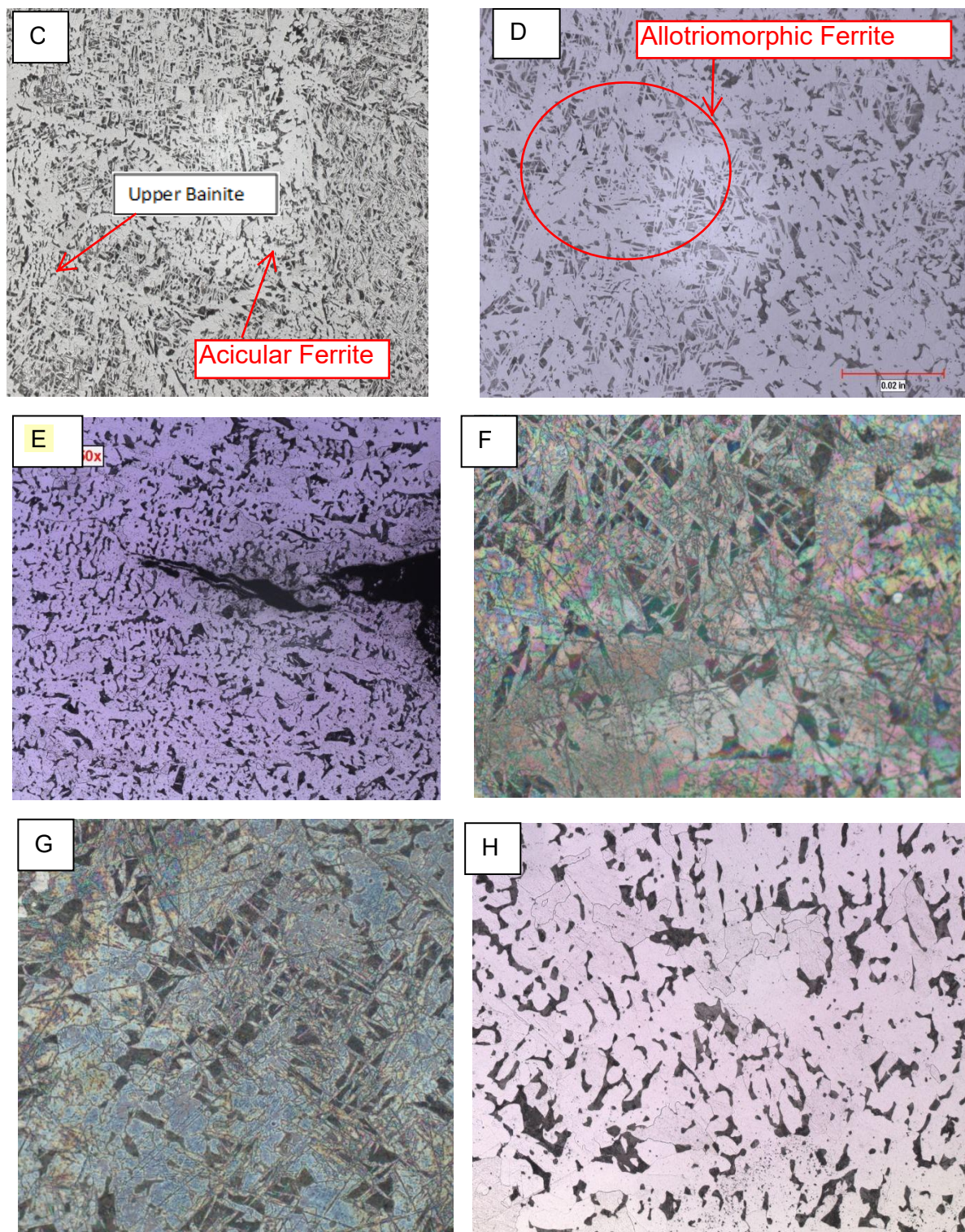


Figure 1: (A – H) The micrographs A through H show various areas from the low carbon steel that cooled in air upon break out during continuous casting. (B) shows more ferrite and a film of cementite (white) around the pearlite. The rest of the micrographs (C through H) show typical as-cast microstructures at various stages of solidification; the dendrites of the columnar zone (F and G), acicular ferrites (C), polygonal ferrites and allotriomorphic ferrite (H).

3.3 SEM – EBSD

A sample supplied to the third-party laboratory was already polished to 1 micro surface finish. But since EBSD (Electron Backscatter Patterns) originate from depths on the order of tens of nanometers of a sample the said sample needed more

polishing. The sample contained a large void extending through its thickness with smaller voids on the polished surface. In order to avoid polishing media from filling the voids, they were filled with EpoThin™ epoxy using a syringe. The epoxy was allowed to cure overnight.

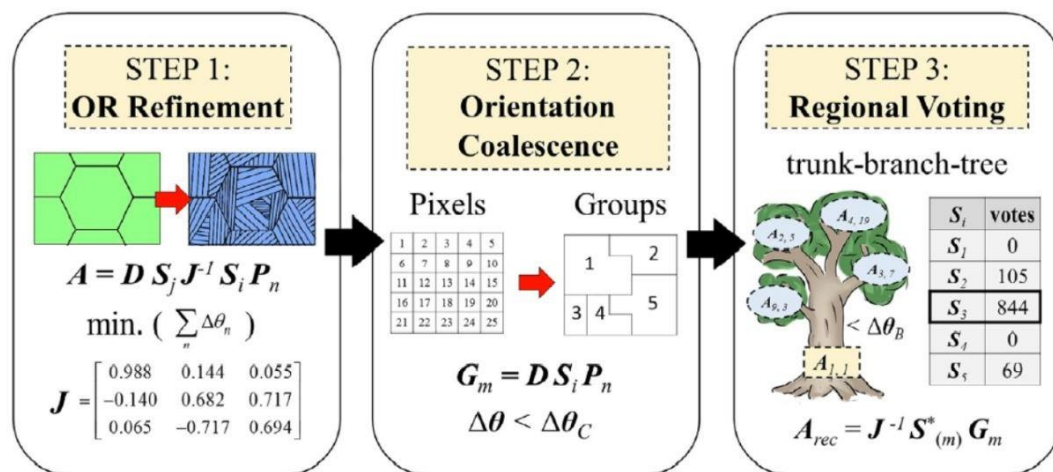
Sample was then polished using 1200 grit SiC paper followed by 3 μm , 1 μm , and 0.25 μm diamond paste. A triple ion beam (argon) polisher was used as the final polishing step. EBSD mapping was performed before the he SEM/EDS analysis to avoid the possibility of carbon being deposited on the newly polished surface during SEM/EDS analysis. The maps were obtained at 250X (field of view approximately 0.51 mm x 0.39 mm) from two different areas a few weeks apart.

3.4 Theory of Parent Grain Reconstruction

Phase transformation occurs through the operation of an orientation relationship (OR). According to Bhadeshia an OR refers to the coherent geometric parallelism between specific planes and directions of parent-child crystal symmetries on either side of their common boundary segment. In all parent-child crystal symmetry combinations, one or more favored ORs exist that provide the best fit at their boundary segment interfaces and enable crystallographic phase transformation between them [13].

Orientation relationships (OR) occur in both displacive (Diffusionless - like martensitic) transformations and diffusion (growth-based transformation occurring at high temperatures). Diffusion based transformations often involve chemical atomic transfers and so chemical composition differences which could result in the loss of atomic correspondence between parent and daughter.

For either case the theory behind their (OR) computation has evolved from solving rigorous manual mathematical Rotation Matrices as detailed in Bhadeshia to the use of digital computational analysis. In their work, Cheng-Yao Huang et. al. devised a 3-step process (see Fig. 2) for parent grain reconstruction involving (i) the refinement of the orientation relationship, (ii) Orientation Coalescence and (iii) a voting process [13-16]. These steps are really better described by the authors than we could. They depicted the said processes graphically as hereunder:



Graphical representation of the 3-step parent grain reconstruction approach of Huang et al. (2020)

Figure 2: Orientation maps showing the benefit of orientation refinement for the successful parent grain reconstruction in martensite.

The major motivation in this portion of the study derives from interest in the crystallographic information that could be obtained and used for understanding prior austenite grain boundary in low carbon steels. Even though most of the reconstruction calculations have been based on Austenite (FCC) to Martensite (TCP) structures and vice versa, this work utilizes only acicular ferrite and bainitic microstructures that resulted from the transformed low carbon in this alloy (0.14Wt.%C max).

Diffusionless transformation from austenite (γ) to martensite (α') occurs according to a fixed crystallographic orientation relationship (OR). Up to 24 orientational variants may satisfy the OR in this situation. X- ray diffraction had been used to identify ORs in mild steel, by Kurdjumov-Sachs (KS) [15-18].

$$\{111\}_{\gamma} // (011)_{\alpha'}; \langle \bar{1}01 \rangle_{\gamma} // \langle \bar{1}\bar{1}1 \rangle_{\alpha'}$$

Nishiyama-Wassermann¹⁸ (NW) obtained OR relationships in Fe 30%Ni alloys

$$\{111\}_{\gamma} // (011)_{\alpha'}; \langle \bar{1}\bar{1}2 \rangle_{\gamma} // \langle 0\bar{1}1 \rangle_{\alpha'}$$

This transformation from austenite (parent) to martensite (daughter) is usually achieved by quenching or rapid cooling from a high temperature[17,18]. In martensitic transformation, there are 24 equivalent variants of martensite capable of forming one prior austenite grain based on transformation crystallography, or orientation relationship (OR). Ideally these 24 variants would occupy the prior austenite grain in the same volume fraction [14, 15].

Patterns were studied from two (indexed) spots of one sample using the electron beam backscatter. Since EBSPs originate from depths on the order of the top tens of nanometers of the sample, samples were polished several times for EBSD mapping as already described above. Electron backscatter diffraction orientation data from commercial software are typically in the

form of a set of Euler angles for each X, Y, and Z positions on the sample surface. Such EBSD data were therefore collected in this study.

The map acquisitions were set up to index both the BCC and the FCC phases of steel. No meaningful number of FCC patterns were indexed for either map (patterns indexing as FCC comprised approximately 0.02% to 0.08% of the total patterns indexed), therefore, the data were reprocessed using only the BCC phase. Typical data from both the BCC and FCC and the BCC only maps are presented below for Map Area 1 and Map Area 2.

EBSD Map Area 1: Maps, Pole Figures, and Grain Size Charts are presented.

Phase	a	b	c	Alpha	Beta	Gamma	Space Group	Database
Fe-BCC	2.87 Å	2.87 Å	2.87 Å	90.00 °	90.00 °	90.00 °	229	OINA Phases
Fe-FCC	3.66 Å	3.66 Å	3.66 Å	90.00 °	90.00 °	90.00 °	225	OINA Phases
Silicon	5.43 Å	5.43 Å	5.43 Å	90.00 °	90.00 °	90.00 °	227	HKL

Table 1: Phases for Acquisition -Showing Space Group and Databases used in Area 1.

In Table 1 above we present the data bases used for the indexing. It shows the typical lattice parameters for Fe- BCC, Fe - FCC and Silicon and the corresponding Space Groups.

Study of Fig. 3 below shows the EBSD color map of phases present. The preponderance of RED COLOR indicate the dominance of the Fe-BCC over the minuscule Blue representing the Fe-FCC in the layered EBSD image.

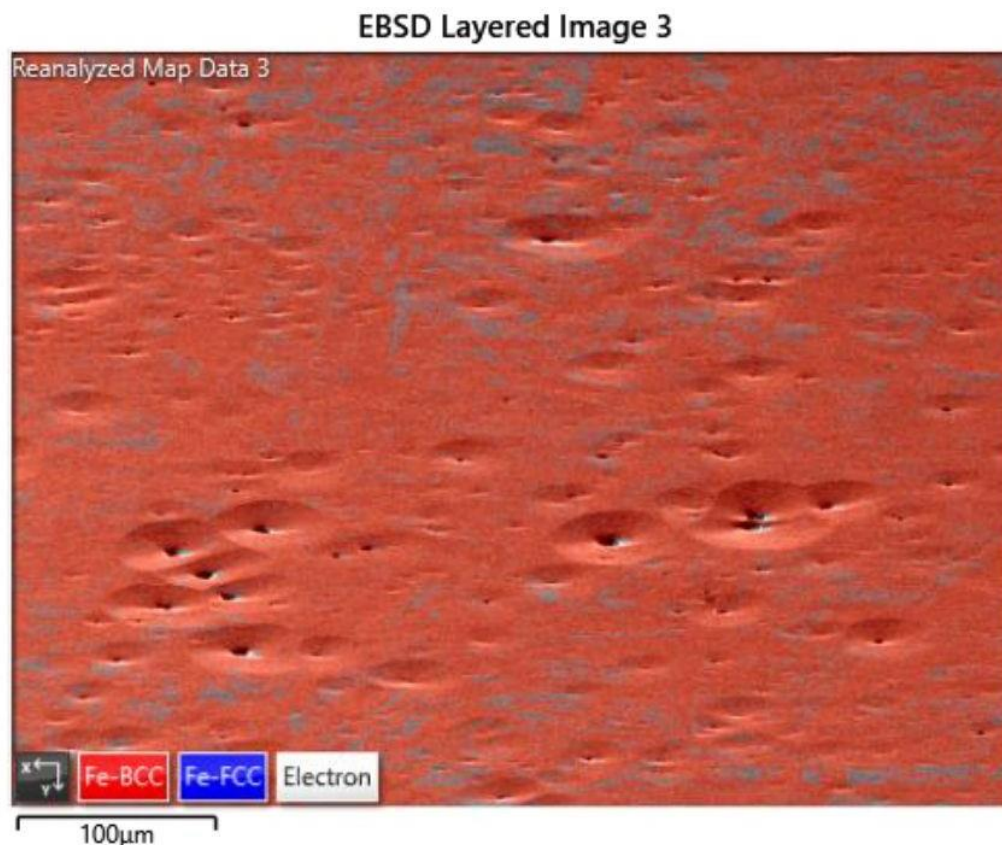


Figure 3: EBSD Layered image map showing the Fe-FCC (Blue) and Fe – BCC in Red

Figures 4 through 6 below show color spatial distribution of Euler angles in both Pole fractions or Inverted Pole Fractions as indicated below each figure. For each figure there is an accompanying color legend for ease of understanding.

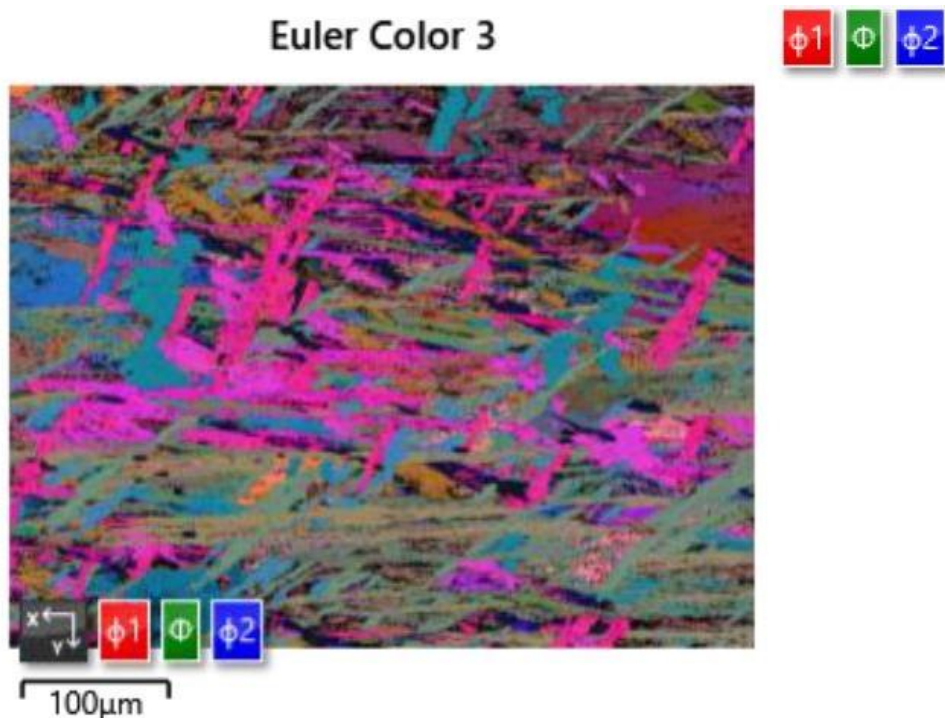


Figure 4: Spatial distribution of Orientation of Euler angles. Legend is in corresponding colors.

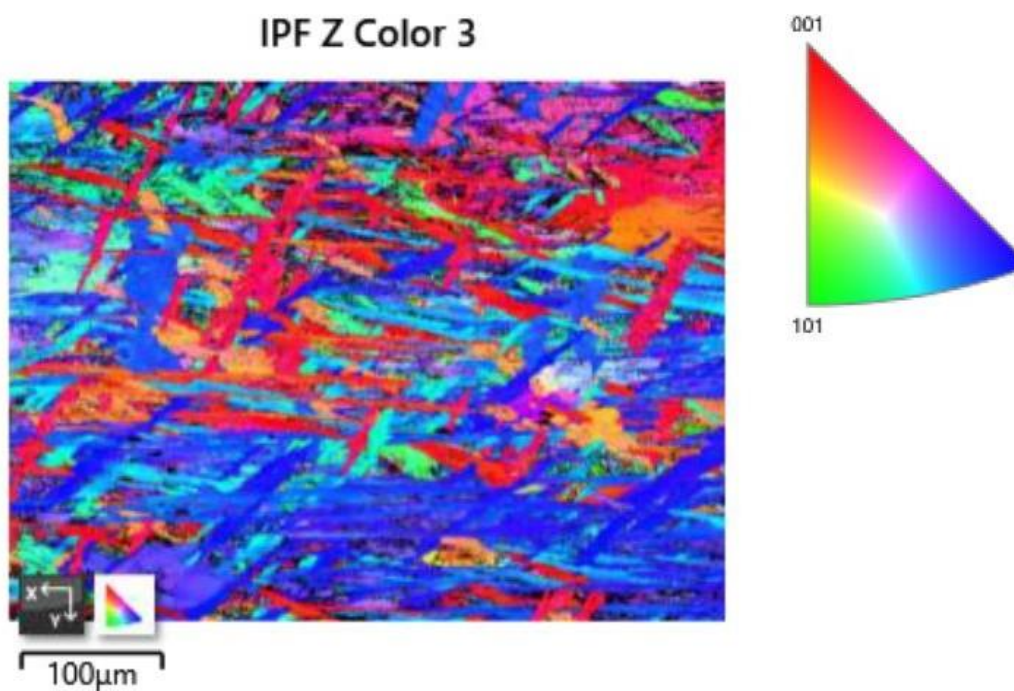


Figure 5: Spatial distribution of the Inverse Pole Fraction crystallographic orientations as seen in the Z - direction

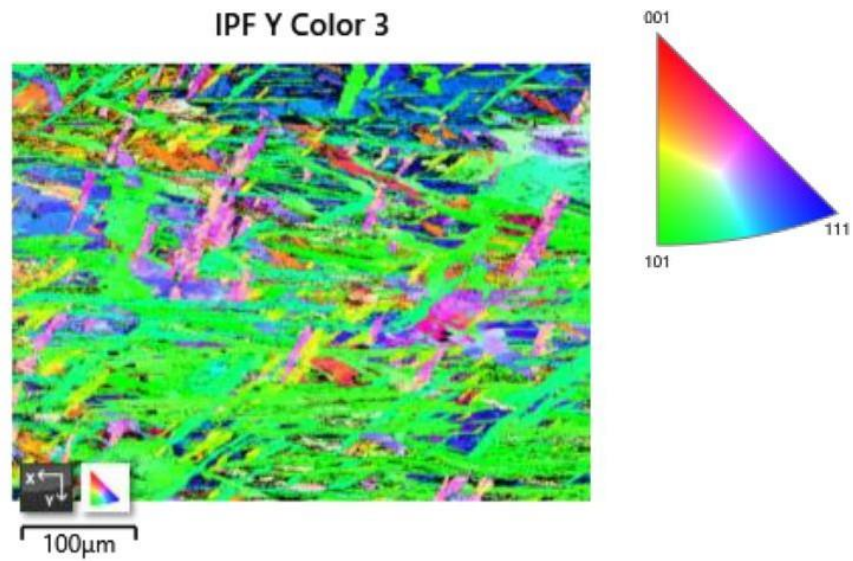


Figure 6: Spatial distribution of the Inverse Pole Fraction crystallographic orientations as seen in the Y - direction

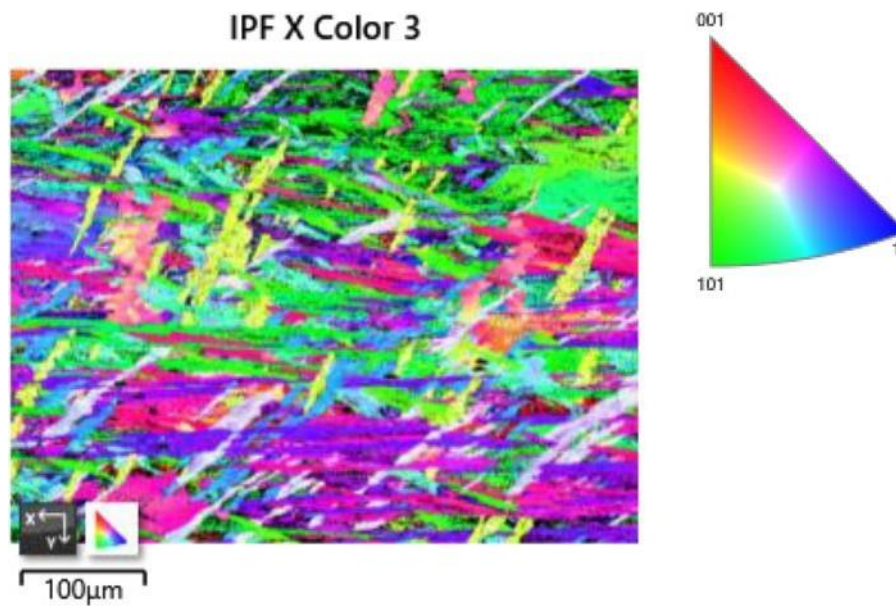


Figure 7: Spatial distribution of the Inverse Pole Fraction crystallographic orientations as seen in the X - direction

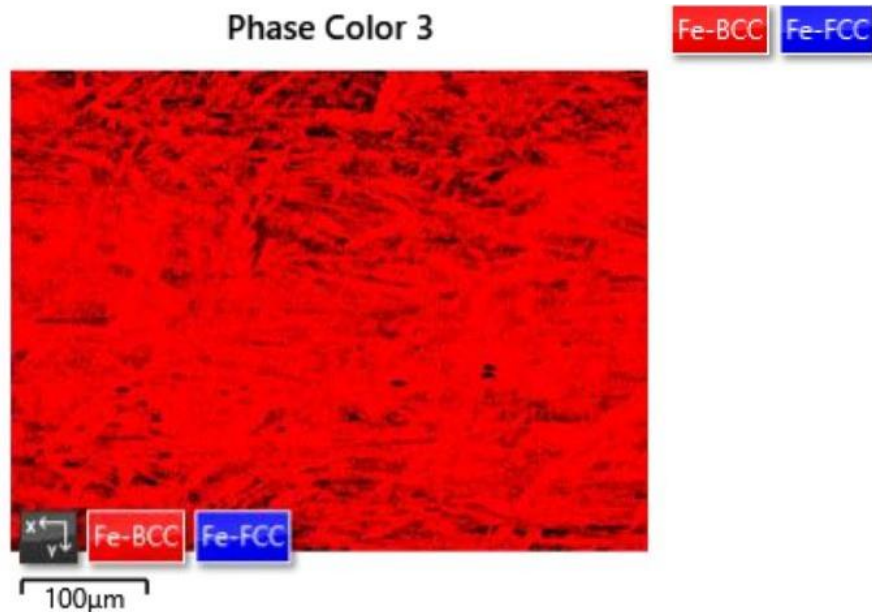


Figure 8: Phase Map from Sample Spot 2 showing Fe-FCC (Blue) and Fe- BCC (Red)

Phase Name	Phase Fraction (%)	Phase Count	Mean Band Contrast	Standard Deviation Band Contrast	Min Band Contrast	Max Band Contrast	Mean MAD	Standard Deviation MAD	Min MAD	Max MAD
Fe-BCC	85.36	466334	75.09	15.87	16.00	133.00	0.91	0.21	0.20	2.00
Zero Solutions	14.64	80008	43.16	12.29	0.00	136.00				
Phase Name	Reanalysis Fraction (%)	Reanalysis Count	Mean Band Contrast	Standard Deviation Band Contrast	Min Band Contrast	Max Band Contrast	Mean MAD	Standard Deviation MAD	Min MAD	Max MAD
Fe-BCC	85.36	466334	75.09	15.87	16.00	133.00	0.91	0.21	0.20	2.00
Zero Solutions	14.64	80008	43.16	12.29	0.00	136.00				

Table 2: Showing Percentage Phase Fractions obtained from Area 1 of Sample indexed

It is noticed that the most of the percentage fraction indexed is Fe-BCC (85.36%) as against the Fe-FCC which is actually in the ZERO solution domain with 14.84%. This is to be expected from a slow cooled liquid steel sample associated with a steel break out process.

POLES

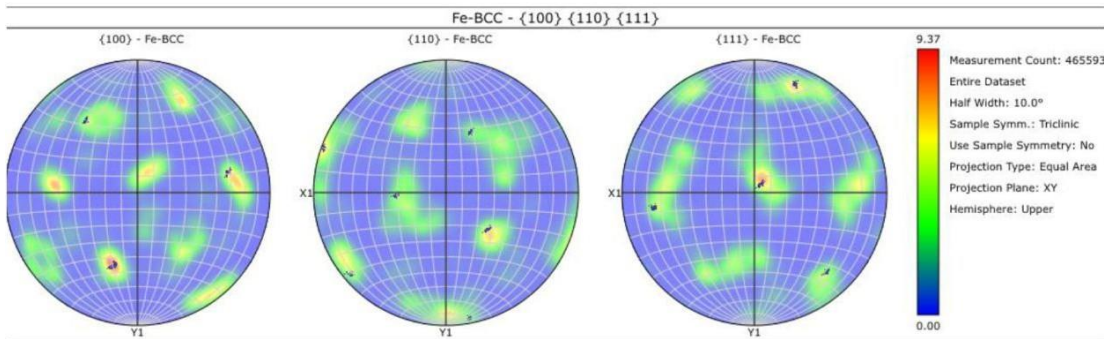


Figure 9: Showing the Poles for the BCC

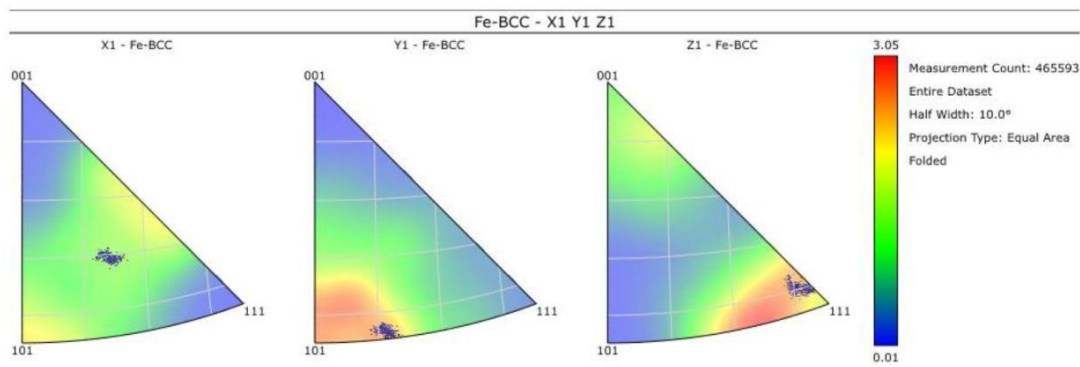


Figure 10: Shows - Map 1 Inverse Pole Figures for Sample indexed as BCC. Grain Size Chart

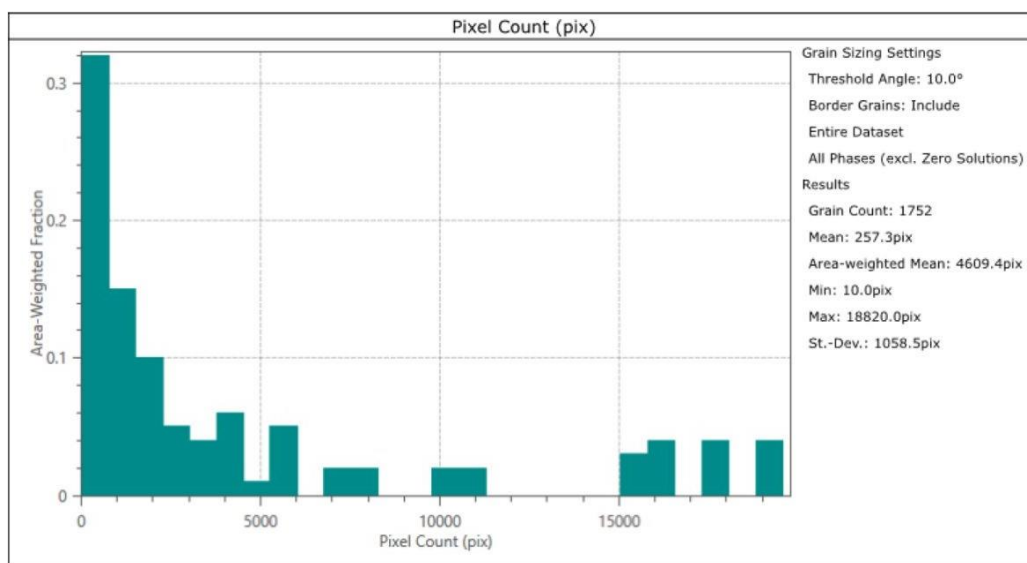


Figure 11: Shows the Grain Size Chart for Map 1.

Map Area 2

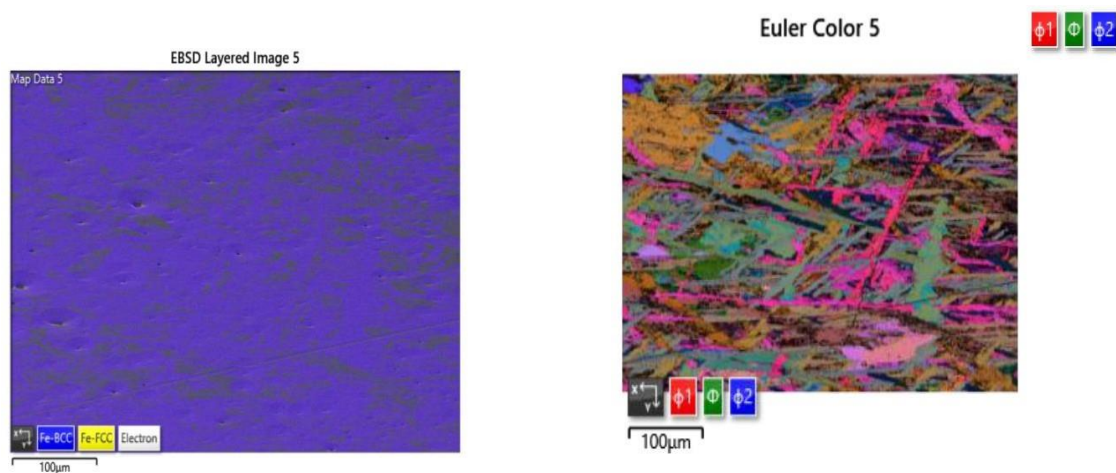
Corresponding findings for Pole Figures, Grain Size Chart and Maps are as hereunder. Again the phases for acquisition are tabulated below, in TABLE 3.

Phases for Acquisition

Phase	a	b	c	Alpha	Beta	Gamma	Space Group	Database
Silicon	5.43 Å	5.43 Å	5.43 Å	90.00 °	90.00 °	90.00 °	227	HKL
Fe-BCC	2.87 Å	2.87 Å	2.87 Å	90.00 °	90.00 °	90.00 °	229	OINA Phases
Fe-FCC	3.66 Å	3.66 Å	3.66 Å	90.00 °	90.00 °	90.00 °	225	OINA Phases

Table 3: Showing the Space Group and Databases used in Area 2 of the Indexed Sample

The following Map Images were determined:



Euler colors for IPF Z, Y and X Color 5 are also shown below:

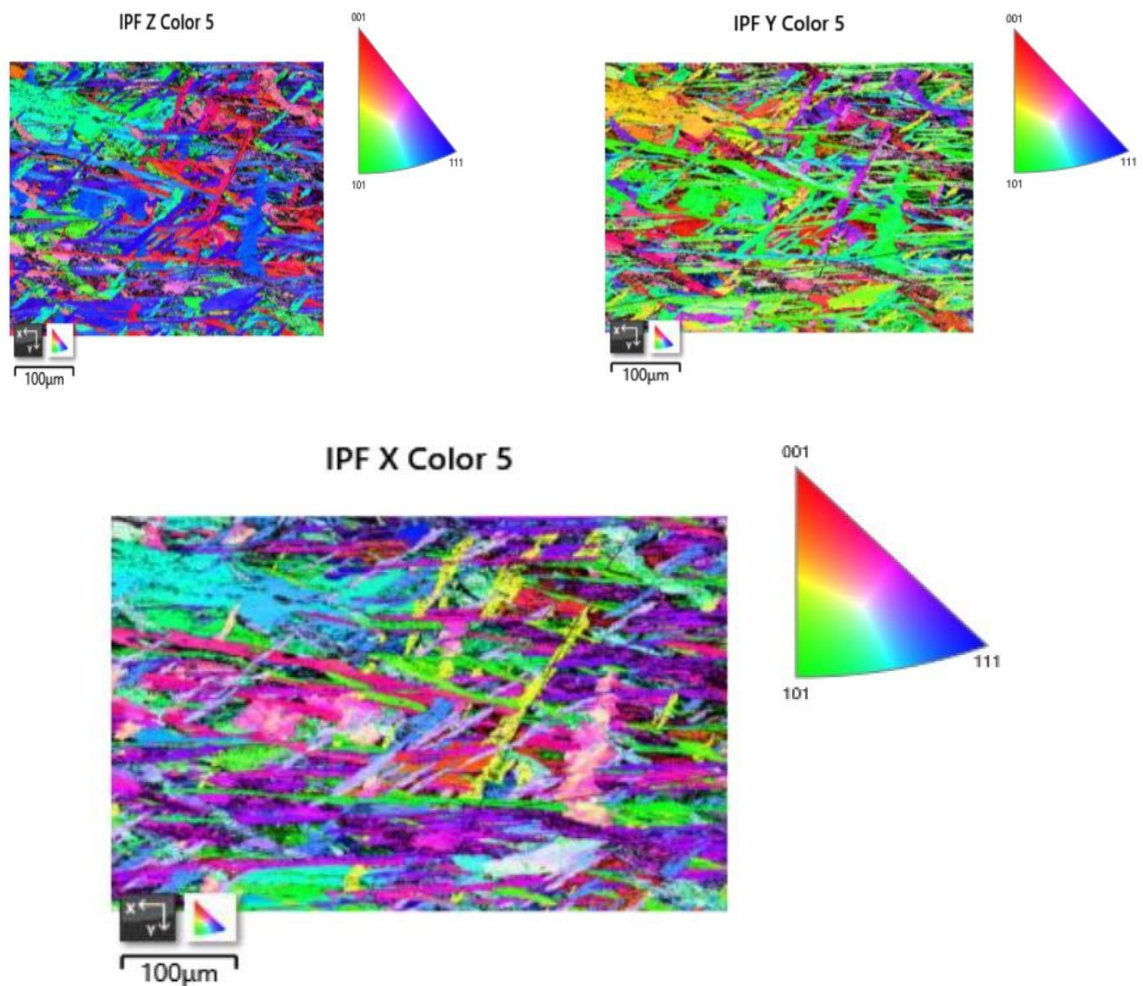


Figure 12: Shows 4 No. Euler Colors for different directions in different planes, (X, Y and Z.) Finally the following Phase Fraction Phase Acquisition data were obtained.

Phase Fraction

Phase Name	Phase Fraction (%)	Phase Count	Mean Band Contrast	Standard Deviation Band Contrast	Min Band Contrast	Max Band Contrast	Mean MAD	Standard Deviation MAD	Min MAD	Max MAD
Fe-BCC	78.67	626365	77.24	17.27	10.00	152.00	0.93	0.24	0.15	2.00
Fe-FCC	0.01	108	58.27	23.74	19.00	131.00	1.22	0.34	0.43	1.96
Zero Solutions	21.32	169767	41.22	14.42	0.00	207.00				

Table 4: Showing Percent Phase Fractions obtained from Area 2 of the Indexed Sample.

As observed in area 1, the percent fraction of Fe-BCC (78.67%) is dominant in area 2 as against Fe-FCC (0.01%) Zero solutions were estimated as 21.23%. This makes Fe- FCC presence here none existent.

Phases obtained from a third Area which was just picked to verify consistency gave rise to the following phase fraction and corresponding Pole data in Table 5 below .

Phase Fraction

Phase Name	Phase Fraction (%)	Phase Count	Mean Band Contrast	Standard Deviation Band Contrast	Min Band Contrast	Max Band Contrast	Mean MAD	Standard Deviation MAD	Min MAD	Max MAD
Fe-BCC	85.25	678788	74.05	14.93	16.00	135.00	1.02	0.20	0.19	2.00
Zero Solutions	14.75	117452	42.62	12.24	0.00	179.00				
Phase Name	Reanalysis Fraction (%)	Reanalysis Count	Mean Band Contrast	Standard Deviation Band Contrast	Min Band Contrast	Max Band Contrast	Mean MAD	Standard Deviation MAD	Min MAD	Max MAD
Fe-BCC	85.29	677260	74.04	14.93	16.00	135.00	1.02	0.20	0.19	2.00
Zero Solutions	14.71	116816	42.62	12.21	0.00	179.00				

Table 5: Showing Percent Phase Fractions obtained from a Third area of same sample.

Consistent with the two previous area 1 and 2 the third area yielded mostly Fe- BCC percent Fraction (85.29%)

POLES

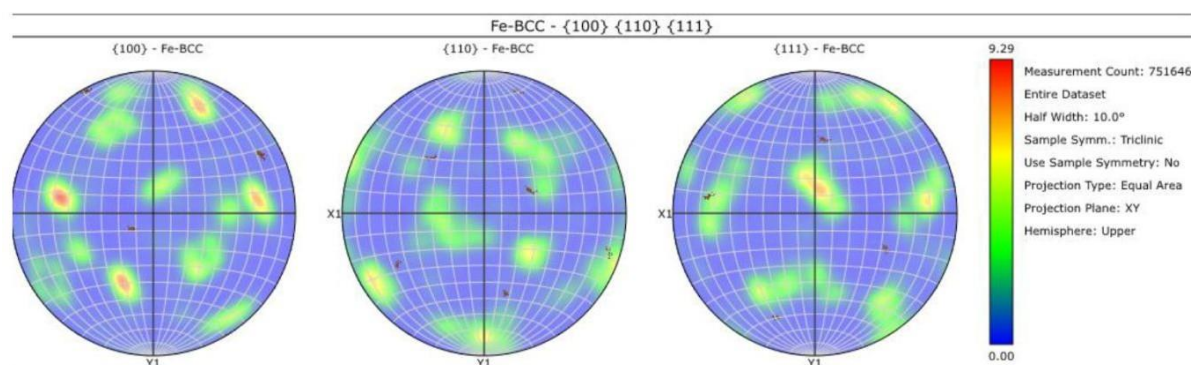


Figure 13: Shows the POLES for BCC in Map 2.

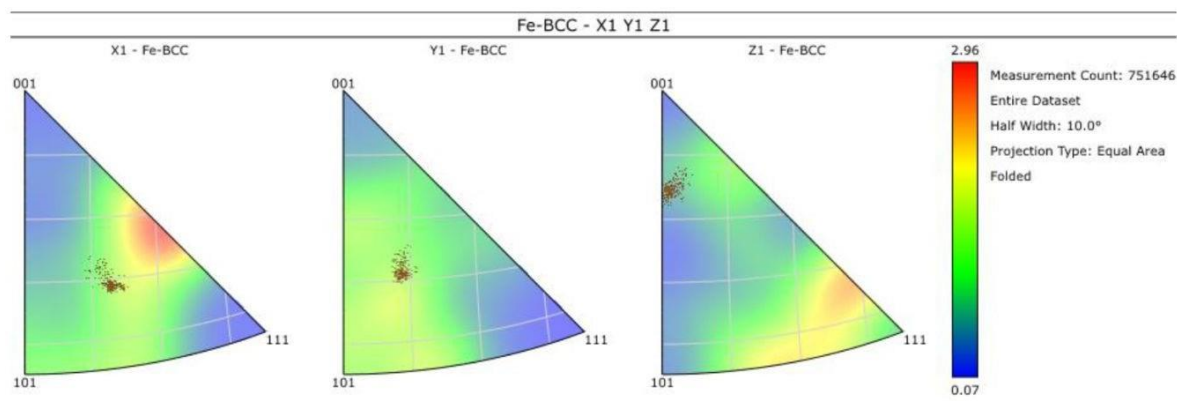


Figure 14: Shows the Map 2 Inverse Pole Figures for Sample indexed as BCC

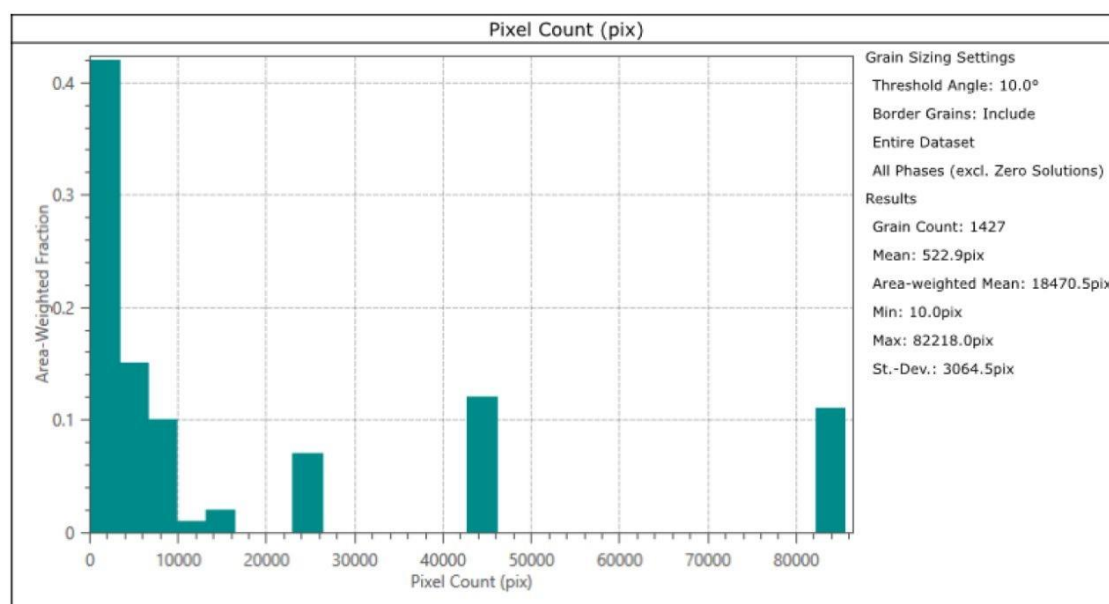


Figure 15: Shows the Pixel Count for area Map 2.

3.4 Parent Phase Reconstruction

An attempt was made to reconstruct the parent phase from the BCC data obtained in this study using the Aztec Crystal software. The austenite grain has a specific orientation relationship with the ferrite matrix derived from it. Grains that have been formed by a $\alpha - \gamma$ or vice-versa phase transformation should show a Bain, Nishiyama - Wassermann (N-W), or Kurdjumov-Sachs (K-S) orientation relationship. These orientation relationships can be described as a rotation of an angle Φ about a common crystallographic axis (axis of rotation). This angle and axis are known as the angle/axis pair. Table 1 shows typical Orientation relationships between austenite (γ) and ferrite (α) matrix.

In this work, a Nishiyama – Wassermann relationship was used.

Typically, one can see the outline of the parent grains which allows one to “train” the software to interpret the child/parent relationship(s). But there were no apparent parent outlines, suggesting that the size of the parent grains were significantly larger than the map area. It is perhaps pertinent to point out that the sample was from a breakout heat at high casting temperatures. These high temperatures create large austenitic grain sizes as opposed to a rolled sample piece, which could have smaller austenitic parent grains. In theory, one should still be able to process the data, but it did not seem to create the expected singular parent orientation. Much of the results obtained with our data is shown below. The blue segmentation represents the FCC Parent Phase.

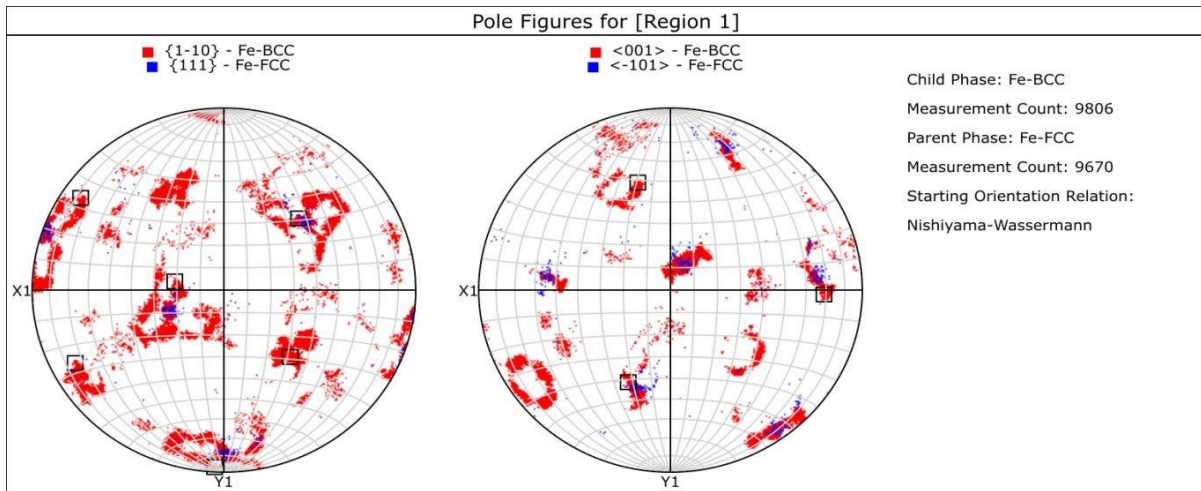


Figure 16: Shows Pole figures for Region 1 indicating both the Child Phase (BCC) and Parent Phase (FCC)

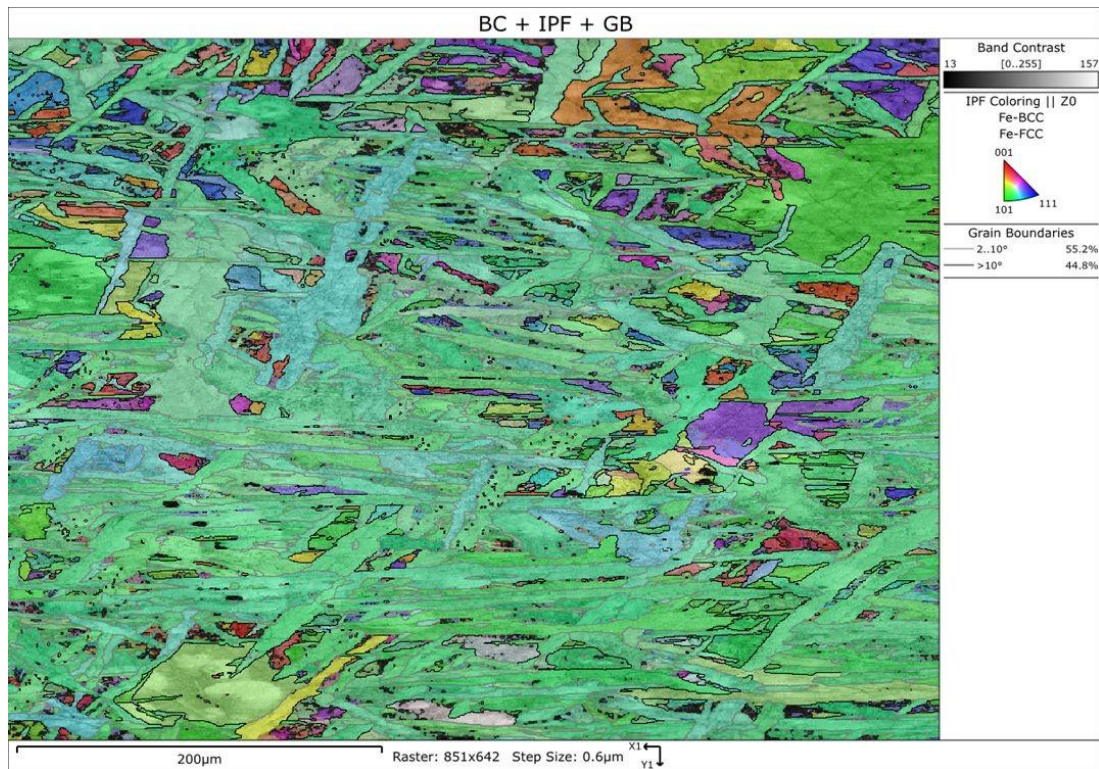


Figure 17: Shows the Band Contrast, Inverse Pole Figure and Grain Boundary; with Corresponding Angles (2 – 10 degrees) producing 55.2% of the GB while angles larger than 10 degrees accounted for 44.8%

TABLE 6. Typical Orientation relationship between planes and Misorientation angle/axis.

Orientation relationship	Lattice correspondence relation	Misorientation angle/axis
Bain	$\{001\}\gamma // \{001\}\alpha$ $\langle 110 \rangle\gamma // \langle 110 \rangle\alpha$	$45^\circ / \langle 001 \rangle$
Kurdjumov-Sachs (K-S)	$\{111\}\gamma // \{011\}\alpha$ $\langle 011 \rangle\gamma // \langle 111 \rangle\alpha$	$42.8^\circ / \langle 2\ 2\ 11 \rangle$
Nishiyama-Wassermann (N-W)	$\{111\}\gamma // \{011\}\alpha$ $\langle 112 \rangle\gamma // \langle 011 \rangle\alpha$	$45.9^\circ / \langle 254 \rangle$

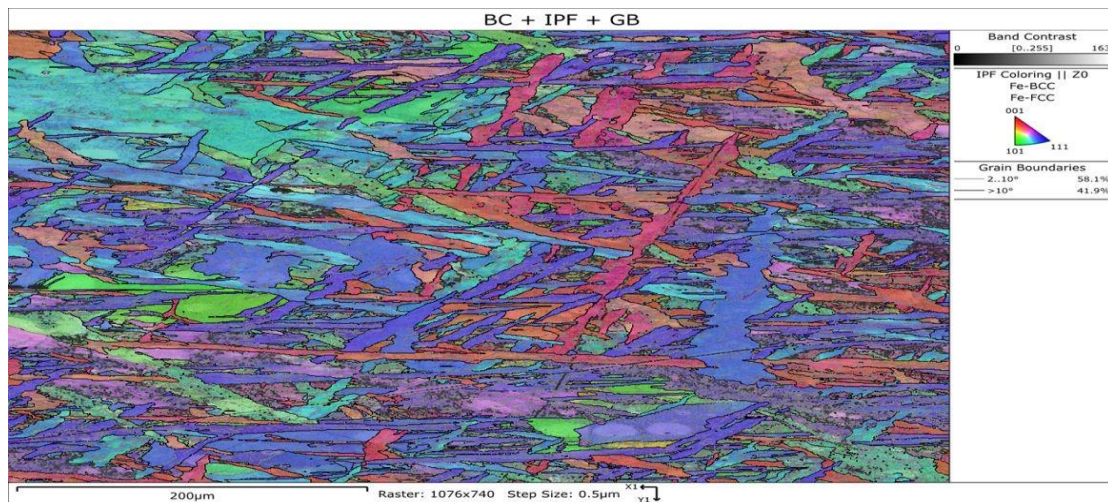


Figure 18: Shows the Band Contrast, Inverse Pole Figure and Grain Boundary; with Corresponding Angles (2 – 10 degrees) producing 58.1% of the GB while angles larger than 10 degrees accounted for 41.9%

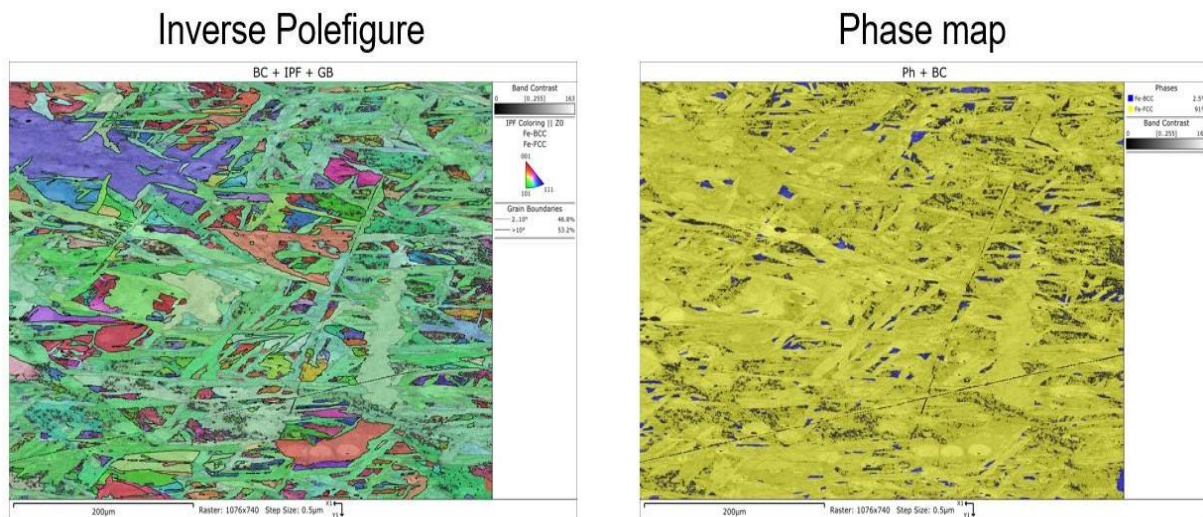


Figure 19: Shows the Band Contrast, Inverse Pole Figure and Grain Boundary on the left. On the right is the Phase Map, showing 2.5% BCC and 91% FCC.

3.5 Discussion

Kengo HATA et. al. reported in their work, using the theoretical approach, where tolerance angles were set at various angles within the range of 2–15 degrees [18]. They continued the analysis when the misorientation θ was within the tolerance angle. The result is shown in Fig. 20 below.

In their work Kengo HATA reported that when the tolerance angle was set at 2 degrees (Fig. 20(a) below), the analysis failed to discover any common austenite orientation with adjacent variants. Therefore, no grain is shown in the figure. This is because the tolerance angle is set too low to discover a common austenite orientation. When the tolerance angles are 3 degrees or above, martensite variants having a common austenite

orientation were discovered. They further reported that its region expanded greatly as the tolerance angle is increased. These results clearly indicate that the analysis of common austenite

grains can vary depending on the tolerance angle. The group of plots shown below (Fig. 20) are taken from the work of Kengo HATA et al. for clarity.

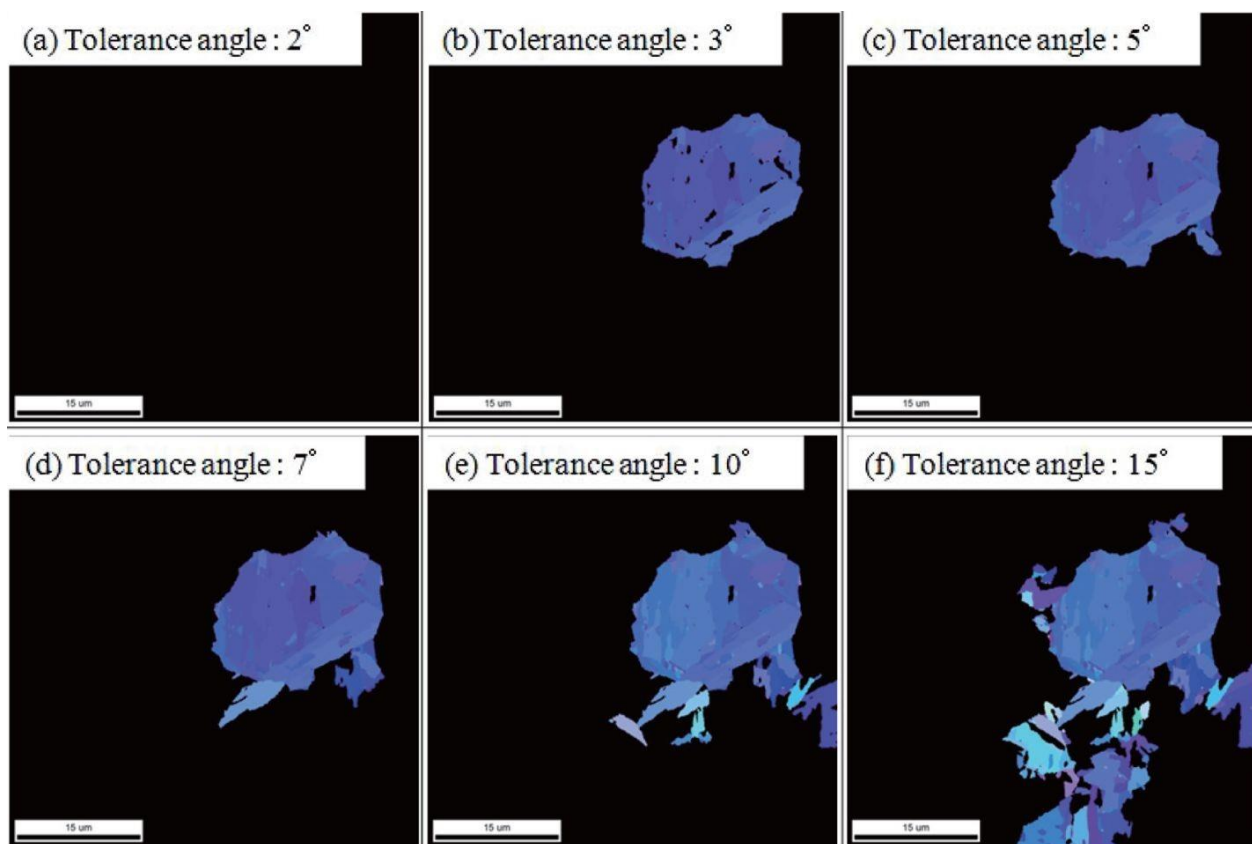


Figure 20: Group of variants with common prior gamma orientation for different tolerance angles indicated as orientation mapping (Work of: Kengo HATA, Kazuki FUJIWARA, Masayuki WAKITA and Kaori KAWANO, Ref. 18)

In the same work, Kengo HATA et. al. artificially computer generated fifty thousand pairs of crystal orientations that do not have any crystallographic relationship with one another and studied the probability of obtaining a common austenitic relationship between them. A plot of this probability versus tolerance angle is reproduced below [18].

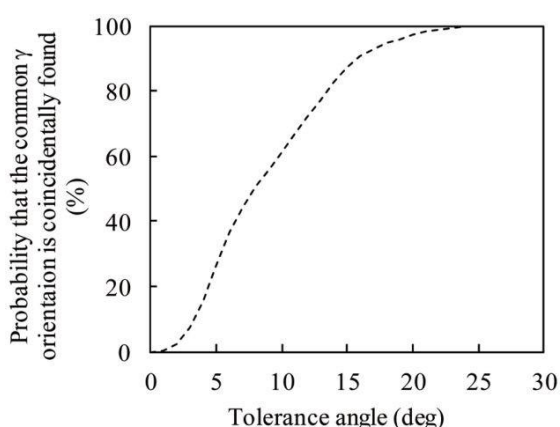


Figure 21: Probability of finding coincidental common gamma angle versus Tolerance Angle Relationship, (Ref. 19).

The plot reveals that at low tolerance angles the probability that a common gamma orientation is found is truly low. It is suggested that our inconsistency in the results of prior austenite analysis at different tolerance angles may be due to low tolerance angle and thus the high probability of NOT discovering common austenite

orientation variants that have been transformed from different austenite grains.

4. Conclusion

1. Optical Microscopy studies were performed on several

samples from a breakout low carbon steel heat.

2. The microstructure was as expected mostly acicular ferrite, polygonal ferrite and allotomorphic ferrite.
3. SEM/EDS and EBSD analysis were used to determine the grain size, phase fractions and Orientation Relationships (OR) of the grains present.
4. The sample was mostly comprised of alpha ferrite phase.
5. Data from EBSD were used to determine Prior Austenite Grain Boundary and the result was not sufficient to generate a lot of grains because the initial scan area was small, and the pole figures suggest possible one or two grains there from.

Acknowledgements

The authors acknowledge the invaluable discussions / assistance received from Prof. Hung-Wei (Homer) Yen of The National University of Taiwan. His very experienced contributions in discussions are truly appreciated. The selfless contributions of Sam Pennington and Richard McLaughlin of Oxford instruments are gratefully acknowledged. The authors are grateful to Gerdau Long Steel North America for allowing the use of its facilities for this work.

Conflict Of Interest

The authors declare no potential conflict of interest.

References

1. Savage, J., & Pritchard, W. H. (1954). The problem of rupture of the billet in the continuous casting of steel. *Journal of the Iron and Steel Institute*, 178(3), 269-277.
2. T. Mukai, K. Yamaguchi, and S. Ogibayashi: *Tetsu - to - Hagane*, 71 (1985), SI025; *Trans. Iron Steel Inst. Jpn.*, 26 (1986), B163.
3. Cayron, C., Artaud, B., & Briottet, L. (2006). Reconstruction of parent grains from EBSD data. *Materials characterization*, 57(4-5), 386-401.
4. Miyamoto, G., Iwata, N., Takayama, N., & Furuhashi, T. (2011). Reconstruction of parent austenite grain structure based on crystal orientation map of bainite with and without ausforming. *ISIJ international*, 51(7), 1174-1178.
5. Morimoto, T., Yoshida, F., Chikushi, I., Kitahara, H., & Tsuji, N. (2007). Development of variant analysis program by using EBSD data. *Tetsu-to-Hagane*(*Journal of the Iron and Steel Institute of Japan*), 93(9), 591-599.
6. Humbert, M., Moustahfid, H., Wagner, F., & Philippe, M. J. (1994). Evaluation of the high temperature texture of the [Beta] phase of a TA6V sample from the individual orientations of grains of the low temperature [alpha] phase. *Scripta Metallurgica et Materialia*;(United States), 30(3).
7. Humbert, M., & Gey, N. (2002). The calculation of a parent grain orientation from inherited variants for approximate (bcc-hcp) orientation relations. *Journal of applied crystallography*, 35(4), 401-405.
8. MTEX: <https://mtex-toolbox.github.io/index>
8. AztecWave: <https://plus-c.aztecsoftware.com/>
9. S. Bechet, L. Beaujard: *Revue de Metallurgie* Vol. 10 (1995), 830-6.
10. G. Bruckner, A. Köntges and G. Gottstein. (2001). Characterization of the Microstructure of a Breakout Steel Sample. *ISIJ International*, 41(5), 468.
11. Snape, E., & Church, N. L. (1972). Microduplex processing of low alloy steels. *JOM*, 24, 23-29.
12. Kurdjumow, G., & Sachs, G. (1930). Über den mechanismus der stahlhärtung. *Zeitschrift für Physik*, 64(5-6), 325-343..
13. Nambu, S., Shibuta, N., Ojima, M., Inoue, J., Koseki, T., & Bhadeshia, H. K. D. H. (2013). In situ observations and crystallographic analysis of martensitic transformation in steel. *Acta materialia*, 61(13), 4831-4839.
14. Kitahara, H., Ueki, R., Tsuji, N., & Minamino, Y. (2006). Crystallographic features of lath martensite in low-carbon steel. *Acta materialia*, 54(5), 1279-1288.
15. Nishiyama, Z. (1934). X-ray investigation of the mechanism of the transformation from face centered cubic lattice to body centered cubic. *Sci. Rep. Tohoku Univ.*, 23, 637.
16. Wassermann, G. (1935). Über den Mechanismus der $\alpha \rightarrow \gamma$ Umwandlung des Eisens (On the Mechanism of the $\alpha \rightarrow \gamma$ Transformation of Iron). *Mitteilungen aus dem Kaiser Wilhelm Institut für Eisenforschung*, 17, 149-55.
17. Hata, K., Fujiwara, K., Wakita, M., Kawano, K. (2017). *Nippon steel & Sumitomo Metal Technical Report No. 114*, 28.

Copyright: ©2023 Ignatius C. Okafor, et al. This is an open-access article distributed under the terms of the Creative Commons Attribution License, which permits unrestricted use, distribution, and reproduction in any medium, provided the original author and source are credited.